Editors' Suggestion

Quantifying the U 5*f* covalence and degree of localization in U intermetallics

Andrea Marino,[1,2,*] Denise S. Christovam,[1] Daisuke Takegami,[1,3] Johannes Falke,[1] Miguel M. F. Carvalho,[1,4] Takaki Okauchi,[5] Chun-Fu Chang,[1] Simone G. Altendorf,[1] Andrea Amorese,[1,4,†] Martin Sundermann,[1,6] Andrei Gloskovskii,[6] Hlynur Gretarsson,[6,7] Bernhard Keimer,[7] Alexandr V. Andreev,[8] Ladislav Havela,[9] Andreas Leithe-Jasper,[1] Andrea Severing,[4,1] Jan Kuneš,[10] Liu Hao Tjeng,[1,‡] and Atsushi Hariki[5,§]

[1]*Max Planck Institute for Chemical Physics of Solids, Nöthnitzer Straße 40, 01187 Dresden, Germany*

[2]*Institute of Solid State and Materials Physics, TU Dresden, 01069 Dresden, Germany*

[3]*Department of Applied Physics, Waseda University, 3-4-1 Okubo, Shinjuku-ku, Tokyo 169-8555, Japan*

[4]*Institute of Physics II, University of Cologne, Zülpicher Straße 77, 50937 Cologne, Germany*

[5]*Department of Physics and Electronics, Osaka Metropolitan University 1-1 Gakuen-cho, Nakaku, Sakai, Osaka 599-8531, Japan*

[6]*PETRA III, Deutsches Elektronen-Synchrotron DESY, Notkestraße 85, 22607 Hamburg, Germany*

[7]*Max Planck Institute for Solid State Research, Heisenbergstraße 1, 70569 Stuttgart, Germany*

[8]*Institute of Physics, Academy of Sciences of the Czech Republic, Na Slovance 1999/2, 182 21 Prague 8, Czech Republic*

[9]*Department of Condensed Matter Physics, Faculty of Mathematics and Physics, Charles University, Ke Karlovu 5, 121 16 Prague 2, Czech Republic*

[10]*Department of Condensed Matter Physics, Faculty of Science, Masaryk University, Kotlářská 2, 611 37 Brno, Czechia*

(Received 5 April 2024; accepted 26 June 2024; published 15 July 2024)

A procedure for quantifying the U 5*f* electronic covalency and degree of localization in U intermetallic compounds is presented. To this end, bulk sensitive hard and soft x-ray photoelectron spectroscopy were utilized in combination with density-functional theory (DFT) plus dynamical mean-field theory (DMFT) calculations. The energy dependence of the photoionization cross sections allows the disentanglement of the U 5*f* contribution to the valence band from the various other atomic subshells so the computational parameters in the DFT + DMFT can be reliably determined. Applying this method to UGa_2 and UB_2 as model compounds from opposite ends of the (de)localization range, we have achieved excellent simulations of the valence band and core-level spectra. The width in the distribution of atomic U 5*f* configurations contributing to the ground state, as obtained from the calculations, quantifies the correlated nature and degree of localization of the U 5*f*. The findings permit answering the longstanding question why different spectroscopic techniques give seemingly different numbers for the U 5*f* valence in intermetallic U compounds.

DOI: 10.1103/PhysRevResearch.6.033068

I. INTRODUCTION

Intermetallic uranium compounds display a plethora of intriguing phenomena including heavy-fermion behavior, unconventional and spin-triplet superconductivity, hidden and multipolar ordering, singlet magnetism, as well as coexistence of ordered phases [1–4]. It is generally accepted that these phenomena originate from the competition and interplay of U 5*f* local atomiclike correlation effects and the tendency of the U 5*f* to delocalize and form bands. The U 5*f* covalence and degree of localization are hereby key indicators that characterize the system. Yet, the assessment of the electronic structure of these uranium intermetallic compounds is truly challenging since one must go beyond mean-field approaches.

Recent developments based on density functional theory (DFT) combined with dynamical mean field theory (DMFT) provide an exciting opportunity to capture certain aspects of the low- and high-energy properties for a number of U compounds [5–8]. Although achieving very promising results, DFT + DMFT calculations often face the problem of, for example, how to subtract correlation effects already included in both the DFT and the DMFT parts [9] and how to determine the actual magnitude of the correlations. Consequently, accurately reproducing experimentally observed quantities, such as spectra in electron spectroscopy, may pose difficulties if the calculations were to be truly *ab initio*. As a result, the community is facing seemingly conflicting results from different spectroscopic techniques regarding the extent of correlations and the occupation of the 5*f* shell. Examples include the well-known hidden order and unconventional superconductor URu_2Si_2 [10–15], and the recently discovered spin-triplet superconductor UTe_2 [8,16–23].

*Present address: Stellbrink & Partner Patentanwälte mbB Widenmayerstraße 10 80538 Munich, Germany.

†Present address: ASML Netherlands B.V., De Run 6501, 5504 DR, Veldhoven, Netherlands.

‡Contact author: hao.tjeng@cpfs.mpg.de

§Contact author: hariki@pe.osakafu-u.ac.jp

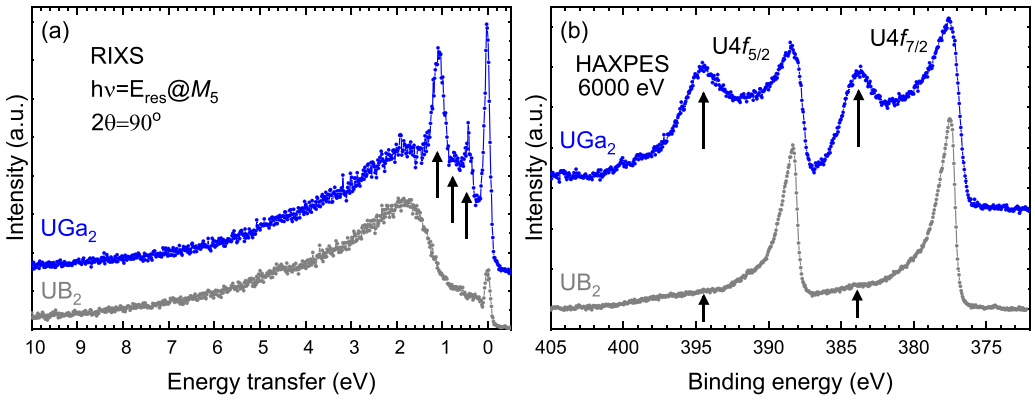

FIG. 1. (a) U M_5-edge RIXS spectra of UGa_2 as adapted from Ref. [24] and of UB_2, both measured at resonance energy. The arrows indicate multiplet excitations. (b) HAXPES U 4f core level spectra UGa_2 and UB_2, after Shirley background subtraction, measured with 6000 eV incident energy. Arrows indicate the satellite structures.

Here we aim to establish a procedure to empirically reduce or even effectively eliminate the uncertainties inherent in DFT + DMFT. Material specific parameters, such as the so-called double counting correction $\mu_{\rm dc}$, the Hubbard $U_{\rm ff}$, and Hund's J of the U $5f$ states, are obtained by tuning the simulation to accurately reproduce the valence band (VB) spectra that are measured with photoelectron spectroscopy (PES) using different photon energies. Measuring the VB with different photon energies allows enhancing or suppressing contributions of the various subshells because their photoionization cross sections depend differently on the incident energy [25–27]; the U $5f$ states contribute most strongly when the VB is measured with soft x rays whereas they are strongly suppressed in hard x-ray spectra. Having disentangled the spectral weights of the subshells, the parameters in the DFT + DMFT calculation can be optimized.

We consider isostructural UGa_2 and UB_2 as model materials that are at the opposite sides of the localization spectrum. UGa_2 is expected to be more atomiclike, while UB_2 must be more delocalized, as inferred from the U–U distances $d_{\rm UU}$ in the their simple AlB_2 hexagonal structure (space group P6/*mmm*) [28–30]. With $d_{\rm UU} = 4.01$ Å, UGa_2 is well above the Hill limit of 3.5Å [31], whereas UB_2 with $d_{\rm UU} = 3.123$ Å is well below. The observed high-moment ferromagnetism (3 μ_B) [32,33] in UGa_2 and the paramagnetic properties of UB_2 down to the lowest measured temperature [34] support this assumption. Furthermore, the VB band resonant inelastic x-ray scattering (RIXS) spectra of UGa_2, measured at the U M_5 edge, exhibit sharp multiplet excitations [see black arrows in Fig. 1(a)]. These excitations were analyzed using a full multiplet approach, which showed that the main configuration is $5f^2$ with Γ_1 and/or Γ_6 symmetry. It was further shown that the large in-plane magnetic moment of UGa_2 is of the induced type, with the Γ_1 singlet being lowest in energy and coupled to the higher-lying Γ_6 doublet [24]. In contrast, the RIXS spectra of UB_2 only show charge transfer scattering, whereas the multiplet excitations are seemingly so strongly broadened that they are no longer distinguishable. Moreover, the U $4f$ core level spectra obtained with hard x-ray photoelectron spectroscopy (HAXPES) exhibit stark differences; in UGa_2, the main emission lines at 378 and 390eV binding energy show prominent satellites, while they are barely visible in the UB_2 core-level data [see black arrows in Fig. 1(b)]. The present core-level data agree well with soft x-ray investigations (see Refs. [35–37] for UGa_2 and Ref. [38] for UB_2). For experimental details of the RIXS and HAXPES data, we refer to Sec. II, Methods, and for further discussion of the spectra we refer to Sec. III, Results, and Sec. IV, Discussion.

This paper aims to provide a quantitative analysis of the charge state of uranium intermetallic compounds. By employing a cross-section guided VB PES study combined with DFT + DMFT calculations, we will determine the charge distribution, the average valence, and the degree of covalence for UGa_2 and UB_2. Using these results, we will *quantitatively* compute the U $4f$ core-level spectra. Additionally, we will discuss the presence and absence of multiplet states in the UGa_2 and UB_2 M_5-edge RIXS spectra, respectively, and address the discrepancies in the interpretation of different spectroscopy techniques concerning the valence states in this material class.

II. METHODS

A. Experiment

UGa_2 single crystals were grown with the Czochralski method and characterized prior to the experiment [39]. Polycrystalline samples of UB_2 were synthesized by arc melting of stoichiometric amounts of crystalline boron (Chempur, 99.95%) together with natural uranium metal (Goodfellow, 99.9%) under a protective atmosphere of Ar gas on a water-cooled copper hearth. The arc-melted sample was placed in an alumina crucible, welded into a tantalum tube and annealed at 1100 °C for 48 hours.

HAXPES measurements were conducted at the P22 beamline [40] at PETRA III (DESY) in Hamburg, Germany. The incident photon energy was set to 6000 eV, thus assuring a higher bulk sensitivity, and photons were detected with a SPECS225HV electron analyzer in the horizontal plane at 90° from the incoming beam, with the sample surface 45° from the incoming beam. Photoelectron spectroscopy with soft x rays (SXPES) was measured with 1200 eV photon energy at the NSRRC-MPI TPS 45A Submicron Soft X-ray Spectroscopy beamline [41] at the Taiwan Photon Source. Here, the photoelectrons were collected by an MB Scientific

A-1 photoelectron analyzer in the horizontal plane at 60° with sample emission along the surface normal. SXPES with 1486.6 eV photon energy were performed with monochromatized Al Kα light in normal emission geometry. Electrons were collected with a Scienta R3000 electron analyzer. In all cases, clean sample surfaces were achieved by cleaving *in situ* in ultrahigh-vacuum condition. The pressures of the main chambers were in the low 10^{-10} mbar range. Valence band spectra of a gold or silver sample were used for calibrating the Fermi level and the overall energy resolution, which was ≈230 meV for the 6000 eV, ≈200 meV for the 1200 eV and ≈300 meV for the 1486.6 eV data. The sample temperature T was kept at 40 K for the 6000 eV and 1200 eV, and at 77 K for the 1486.6 eV measurements.

The RIXS experiments at the U M_5-edge were performed at Max-Planck IRIXS end station of P01 beamline at Petra III/DESY (Hamburg). The RIXS instrument utilizes hard x-ray optics, as described in Ref. [42], and achieves a resolution of 150 meV at the U M_5-edge with the 112 reflection of a diced quartz analyzer, as estimated by measuring a carbon tape. The experiment was performed with a scattering angle $2\theta = 90^o$ to minimize elastic scattering, a sample angle $\theta_s = 45^o$, and $T = 35$ K.

B. Calculations

The valence-band and core-level PES simulations started with a standard DFT + DMFT calculation [43,44] with the local density approximation for the exchange correlation potential. First, the DFT bands for the experimental crystal structure were obtained by the WIEN2K package [45] and subsequently projected onto a tight-binding model spanning U 5f, 7s, 6d orbitals, Ga 4s, 4p, and B 2s, 2p orbitals using the WIEN2WANNIER and WANNIER90 packages [46,47]. The spin-orbit coupling (SOC) was included in the DFT calculation. The tight-binding model was augmented with a local electron-electron interaction within the U 5f shell, parameterized by the Hubbard $U_{\rm ff}$ and Hund's J parameters. The strong-coupling continuous-time quantum Monte Carlo (CT-QMC) impurity solver [48–51] was used to compute the U 5f self-energy, which was analytically continued to real frequency after the convergence of the DMFT self-consistent loop was achieved [52]. For computational efficiency, only the density-density terms in the Coulomb interaction vertex were taken into account in the CT-QMC calculation. The calculations were performed for $T = 300$ K.

Merging the DFT scheme with DMFT faces the well-known problem of how to avoid double-counting the U 5f–5f interaction already present in the DFT results [9,43,53]. To this end, one needs to determine the U 5f site energies by subtracting the so-called double-counting correction $\mu_{\rm dc}$ from the respective DFT values, but a generally accepted universal expression for $\mu_{\rm dc}$ is not available. Practically, $\mu_{\rm dc}$ renormalizes the energy splittings between U 5f and other uncorrelated orbitals.

By successively varying $\mu_{\rm dc}$ in the DFT + DMFT calculations for certain sets of $U_{\rm ff}$ and J, the best agreement of prominent valence-band features in the experimental valence band PES data with the DFT + DMFT spectra determines the $\mu_{\rm dc}$ value for the correction. The double-counting dependence of the valence-band spectra is shown in detail for different sets of $U_{\rm ff}$ and J in Appendix 1.

The core-level PES spectra were calculated from the Anderson impurity model (AIM) augmented with the core states and the real-frequency DFT + DMFT hybridization function discretized into 23 levels (per spin and orbital). For this purpose, we employed the configuration-interaction impurity solver, which allowed us to treat a large number of bath levels (see Refs. [54,55] for details) compared with a standard exact diagonalization solver (see, e.g., Ref. [56]). Nevertheless, treating full U 4f core-orbital degrees of freedom was a computationally demanding task. Thus, s-type ($l = 0$) core orbitals were adopted in the AIM, meaning the SOC splitting on the U 4f core level and the multipole part in the core-valence (U 4f–5f) Coulomb interaction were neglected in the spectra. The U $4f_{5/2}$ and $4f_{7/2}$ SOC splitting is large (∼10 eV) and, consequently, interference effects between the two SOC partners are negligibly small. Thus, only the monopole term $U_{\rm fc}$ in the core-valence interaction had to be adjusted for reproducing the experimental spectra.

III. RESULTS

Figures 2(a)–2(d) show the experimental valence-band PES spectra of UGa_2 and UB_2 measured with soft and hard x-rays. Our low photon energy data agree well with previously reported soft x-ray studies [37,38]. We identify features labeled A to K in the spectra. These features do not shift in energy but exhibit different spectral weights depending on the incident photon energy. In UGa_2, the double peak structure, A (0.15 eV) and B (0.5 eV), is pronounced in the 1200 eV data, while features C (1.11 eV) to F are prominent in the 6000 eV spectrum. It is important to note that feature C has a higher binding energy than feature B. Likewise in UB_2, feature G emerges in the 1486.7 eV data, while the spectral weights of features H to K are enhanced in the 6000 eV dataset.

The energy dependence of the photoionization cross sections [25–27,57] can be exploited to disentangle the different orbital contributions in the valence-band spectra. Figures 3(a) and 3(b) show the photoionization cross sections of the Ga 4s, Ga 4p, B 2s, B 2p, U 7s, U 6d, and U 5f orbitals in the soft and hard x-ray energy range, respectively, with the vertical lines signaling the photon energies used in the experiments. The cross sections generally decrease with increasing photon energy, with the U 5f one always being the largest. However, in the soft x-ray range, the ratio of the U 5f spectral weights to the weights of the other states is at least 3.8 times larger than at 6000 eV. We can thus conclude that the features enhanced in the soft x-ray data, A, B in the UGa_2 spectrum, and G in the UB_2 spectrum, are contributions from U 5f, while all the other features are due to contributions from non-5f states.

Figures 2(e)–2(h) show the optimized DFT + DMFT calculation for the valence band spectra of UGa_2 and UB_2 after weighing the individual orbital intensities with the respective cross sections in Fig. 3 and after some broadening to mimic the respective experimental resolutions. The parameter values of $U_{\rm ff} = 3$ eV, $J = 0.59$ eV and $\mu_{\rm dc}$=4.25 eV reproduce best all the characteristic valence-band features (A–K) at two photon energies simultaneously [compare to Figs. 2(a)–2(d)]. In Appendix 1, we describe the parameter search and

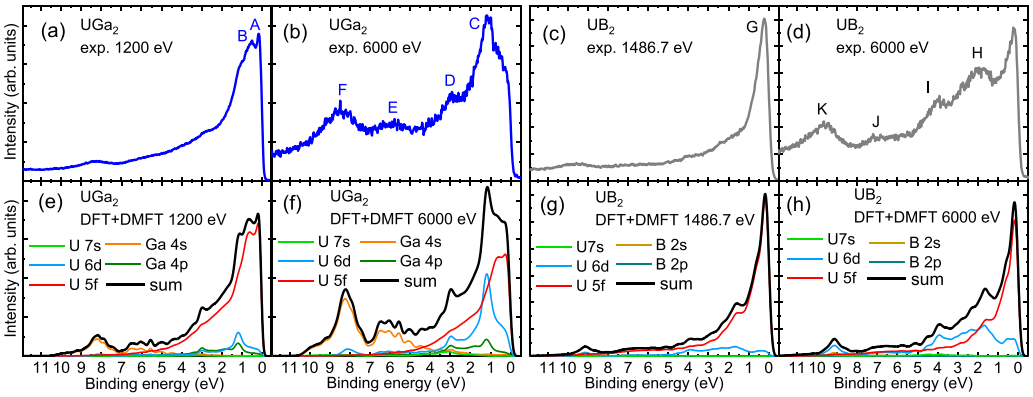

FIG. 2. (a)–(d) Experimental hard and soft x-ray valence band spectra of UGa_2 and UB_2 measured with 1200 eV, 1486.6 eV, and 6000 eV photon energies. (e)–(h) DFT + DMFT calculations of the valence band spectra of UGa_2 and UB_2 for $U_{\rm ff} = 3$ eV, $J = 0.59$ eV, and $\mu_{\rm dc} = 4.25$ eV, after photoionization cross-section corrections (see text) and Gaussian broadening.

demonstrate how the $\mu_{\rm dc}$ parameter scales almost linearly with the relative position of the features originating from the U $5f$ states and the features F and K that come from uncorrelated states. We pick the value of $\mu_{\rm dc}$ that fits best the energy position of features F and K as well as the line shape of the correlated U $5f$ spectrum. The presence of the double-peak features A and B in the U $5f$ states is a manifest of the sizable Hund's J interaction.

The comparison of valence spectra and simulations allows identifying the dominant orbital contributions: features A, B in Fig. 2(a) and G in Fig. 2(c) indeed mainly originate from the U $5f$ states. The intensities C and D in the spectra of UGa_2 mainly come from the U $6d$ and intensities E and F from the Ga $4s$ orbitals. For UB_2 features, H and I are primarily due to the U $6d$, while features J and K also have a sizable B $2s$ contribution.

Given the good agreement of the DFT + DMFT calculations with the valence-band experimental spectra, we now assess the U valence. To this end, we resort to a valence histogram on the uranium site, using the DFT + DMFT method with the optimized material specific parameters. These

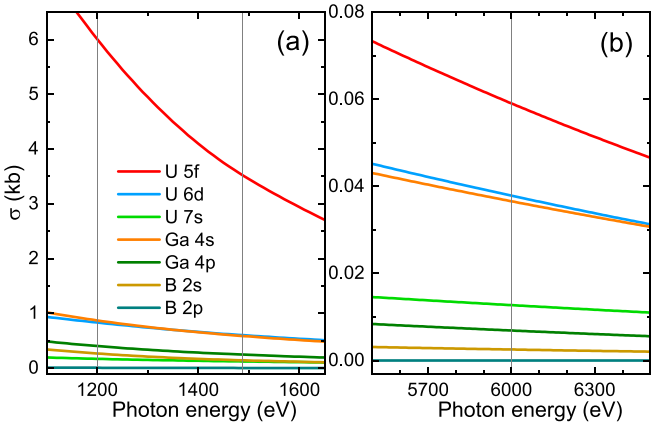

FIG. 3. Photoionization cross sections of U $5f$, U $6d$, U $7s$, Ga $4s$, Ga $4p$, B $2s$, B $2p$ as interpolated from Refs. [25–27]. The vertical lines indicate the photon energies where the experiments were performed.

histograms represent projections of the local density matrix on different $5f$ occupation number sectors. It is computed from the AIM using the numerically exact CT-QMC solver with the DMFT hybridization densities $\Delta(\omega)$. In Figs. 4(a) and 4(b), we present the resulting histograms of UGa_2 and UB_2. It is evident that numerous $5f^n$ atomic configurations contribute to the respective ground states of UGa_2 and UB_2. Thus, the U nominal valence or dominant (starting) configuration for an ionic picture is unclear and is not known *a priori* for U intermetallics. The $\mu_{\rm dc}$ shifts the (bare) U $5f$ energy, and thus has a strong effect on the U valence distribution. A smaller $\mu_{\rm dc}$ results in a shallower U $5f$ level, thereby leading to smaller fillings. We show the variation of the histograms as a function of $\mu_{\rm dc}$ in Appendix 2.

In both histograms of UGa_2 and UB_2, the U $5f^2$ and $5f^3$ configurations are the most prominent. In UGa_2, the $5f^1$, f^2, f^3, and f^4 configurations account for 6%, 66%, 26%, and 2%, respectively, resulting in a filling of the U $5f$ shell of $\langle n \rangle = n_{5f} = 2.24$. In UB_2, the f^0 and f^5 configurations also contribute. We find 1.7% of f^0, 19.2% of f^1, 43.8% of f^2, 28.1% of f^3, 6.4% of f^4, and 0.6% of f^5, resulting in a filling of $\langle n \rangle = n_{5f} \approx 2.20$. Despite the very different physical properties of UGa_2 and UB_2, their *average* $5f$ shell fillings are remarkably similar.

The key distinction between the histograms in Figs. 4(a) and 4(b) lies in the width of the distributions. In UGa_2, the histogram peaks very narrowly around the f^2 configuration, while in UB_2, the distribution is much broader. The width of the histogram carries information about the magnitude of the charge fluctuations, which we find to be significantly larger in UB_2. We also add the statistical (binomial) distribution of the charge configurations that correspond to a completely itinerant uncorrelated f shell [see red ticks in Figs. 4(a) and 4(b)]. The binomial distribution is given by

$$P(f^n) = \binom{14}{n}(1-c)^{14-n}c^n, \qquad (1)$$

where c is the electron concentration $c = n_f/14$. [58]. It shows that atomic correlations are not entirely absent in UB_2 because its DFT + DMFT histogram of UB_2 is still not as broad as the binomial distribution. Nevertheless, the distribution is wide enough so the DFT + DMFT results yield only

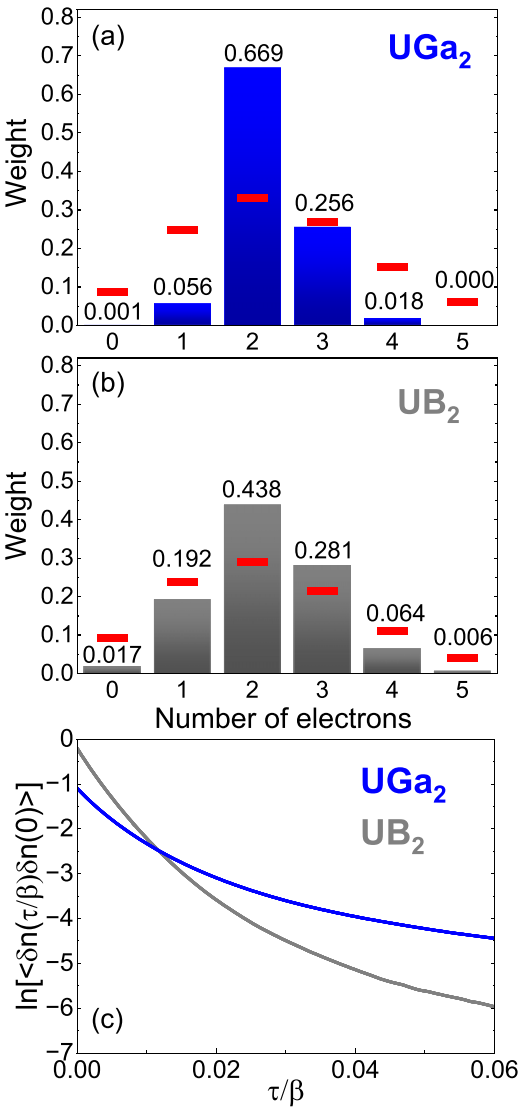

FIG. 4. The atomic configuration histograms of the U 5f states in UGa_2 (a) and UB_2 (b) calculated by the DFT + DMFT method with optimized parameters, $U_{\rm ff}$=3 eV, J=0.59 eV, and $\mu_{\rm dc}$=4.25 eV. The red ticks indicate an uncorrelated statistical distribution of atomic configurations (see text). (c) Logarithm of the time-dependent charge correlation functions $\langle\delta n(\tau/\beta)\delta n(0)\rangle$ of UGa_2 and UB_2 calculated by the DFT + DMFT method.

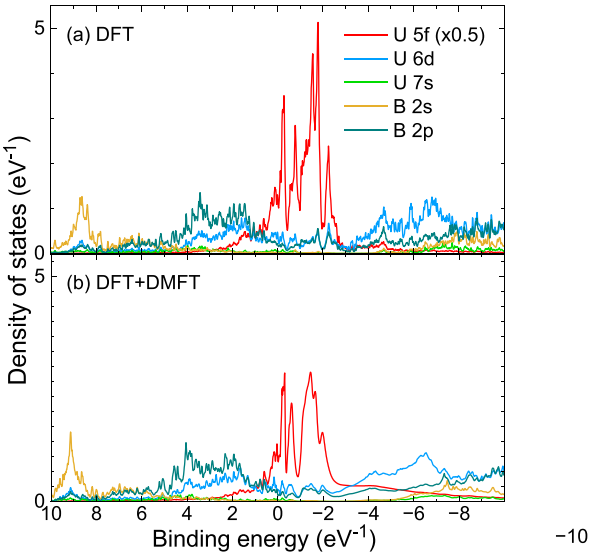

FIG. 5. (a) DFT and (b) DFT + DMFT (with $\mu_{\rm dc}$=4.25 eV) density of states of UB_2.

small spectral changes in comparison to the noninteracting DFT results, as shown in Fig. 5.

Above, we inferred the average 5f occupation n_{5f} as well as the magnitude of charge fluctuations $\langle\delta n\delta n\rangle$ directly from the histograms. However, charge fluctuations can have rather different origins such as itinerancy, i.e., formation of (broad) bands in intermediate valence systems or the degeneracy of valence states—mixed valence. To distinguish these situations, time-dependent charge correlation functions $\langle\delta n(\tau)\delta n(\tau')\rangle$ must be evaluated [59]. In the former case, the correlation function rapidly decays with time $\tau-\tau'$, while in the latter the correlation function contains a long-lived component (in the limiting case of valence degeneracy of isolated atoms, the correlation function remains constant over time). In Fig. 4(c), we show the local charge-charge correlation function $\langle\delta n(\tau)\delta n(0)\rangle$ in the imaginary time domain for UGa_2 and UB_2. We notice that the value of the function at $\tau=0$ is larger for UB_2 than for UGa_2, indicating larger charge fluctuations in the former compound. Moreover, the function decays faster in UB_2, suggesting that the charge fluctuations in this compound are primarily due to itinerancy. For a material even more itinerant than UB_2, the charge correlation function would decay even more rapidly over time (and the histogram resembling more the binomial distribution), whereas for a material even more localized than UGa_2, it would eventually become a constant over time (and the histogram becoming even narrower). Such a comparison would be particularly useful for the relative classification of several other intermetallics.

We now turn our attention to the U 4f core-level excitations of UGa_2 and UB_2, measured with 6000 eV photon energy, after subtraction of a Shirley-type integral background [see in Fig. 1(b)]. Figures 6(a) and 6(b) display the U 4$f_{7/2}$ core-level spectra on an enlarged scale. In the case of UGa_2, a prominent satellite peak is observed at ≈6 eV above the main peak. It is important to note that this feature is not present in the U 5f spectral weight in the valence-band spectra; see Fig. 2(a). In contrast, the spectrum for UB_2 closely resembles that of an (almost) uncorrelated metal: a main, asymmetric peak is observed with minimal to no satellite structure. We then computed the U 4f core-level spectra using the DFT + DMFT AIM [54,55]. The AIM incorporates the DFT + DMFT hybridization densities $\Delta(\omega)$ for the valence-band structure determined above. The sole tuning parameter in this computation is the amplitude of the interaction $U_{\rm fc}$ between the highly localized U 4f core hole generated by the x-rays and the 5f valence electrons. Figures 6(a) and 6(b) show the calculated spectra for both compounds for three values of $U_{\rm fc}$.

An excellent reproduction of the energy positions as well as ratios of main and satellite peaks is achieved with $U_{\rm fc}$=5 eV, which defines this parameters in uranium core-level spectroscopy. It turns out that the core-level data of both compounds are well described with the same set of parameters $U_{\rm fc}$,

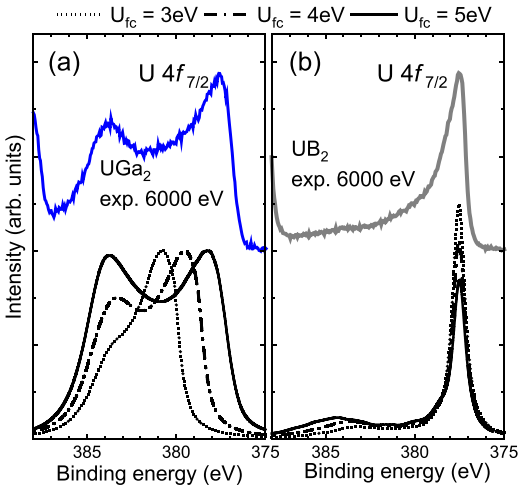

FIG. 6. U $4f_{7/2}$ core-level HAXPES spectra compared to calculations performed with the DFT + DMFT AIM for different core-valence interaction values $U_{\rm fc}$, for UGa_2 (a) and UB_2 (b).

$U_{\rm ff}$, $\mu_{\rm dc}$ and J. Hence, the difference in the spectra comes from the larger itinerancy in UB_2, as revealed by the DFT + DMFT calculation. In Appendix 3, we provide a demonstration of the impact of itinerancy on the core-level spectra.

IV. DISCUSSION

The accurate description of the VB as well as U $4f$ core-level spectra lends credibility to the choice of parameters, especially the double counting correction $\mu_{\rm dc}$, in the present DFT + DMFT calculation. Our results show that the U $5f$ electrons in UB_2 are much more itinerant than in UGa_2. Nevertheless, the U $5f^2$ configuration is the most abundant and the average valence ($n_{5f} \approx 2.2$) is almost identical in both compounds. The latter fact shows how treacherous the qualitative interpretation of U $4f$ core-level data in terms of valence can be (see Appendix 3). The M_5-edge RIXS, on the other hand, do reflect the stronger localization of the $5f$ states in UGa_2 in a very obvious manner: the UGa_2 RIXS data exhibit multiplet excitations, whereas these are washed out for UB_2 due to the significantly larger itinerancy of its $5f$ electrons.

The present results differ from the DFT + DMFT study of UGa_2 by Chatterjee and Kolorenč [56]. Aiming to explain the magnetism, they chose the double-counting parameter $\mu_{\rm dc}$ so the $5f$ filling in the DFT + DMFT result is equal to its DFT value. While Chatterjee and Kolorenč also found a double peak structure close to the Fermi energy, the assignment of features B and C, originating from U $5f$ and other states, respectively, is interchanged [see Fig. 2(a)]. In our paper, the assignment is supported by the strong contrast between SX-PES and HAXPES, the latter enhancing the non-$5f$ spectral weights as shown in Fig. 2(b).

Next we will address the issue of conflicting results from different spectroscopic techniques for U intermetallic compounds. Having established the distinct presence of the electronic configurations involved, as well as having determined the magnitude of the electronic correlation energies $U_{\rm fc}$ and $U_{\rm ff}$, we now are in the position to use the language of configuration interaction to resolve this issue, thereby highlighting a central aspect in the DMFT approach. The histograms presented in Fig. 4 show that multiple $5f$ valence configurations contribute to the ground state, with $5f^2$ and f^3 carrying the largest weight. Therefore, we focus on these two configurations. How does the U $5f$ mixed valence state with $5f^2$ and f^3 configurations, e.g., as in UGa_2, manifest itself in different spectroscopic techniques and why do different techniques seemingly give different answers?

In the following, we consider two typical core-level spectroscopy cases [60–62]: (1) In processes conserving charge neutrality, such as x-ray absorption (XAS) or nonresonant inelastic x-ray scattering (NIXS) at the $M_{4,5}$, $N_{4,5}$, $O_{4,5}$ edges of uranium, the energy ordering of the states originating from the $5f^2$ and f^3 configurations is the same with (final state) and without (initial state) the core hole. The key parameter for the energy order of the final states is the core-valence interaction $U_{\rm fc}$, which is comparable to the valence Coulomb interaction $U_{\rm ff}$. In these charge-neutral processes, where the core-electron excitation takes place locally at the x-ray irradiated site resulting in formation of an exciton, the energy gain attributed to the $U_{\rm fc}$ term is primarily offset by energy loss from the $U_{\rm ff}$. Thus, the perturbation presented by the x-ray irradiation only slightly renormalizes the energy difference of the underlying ionic configurations. In this case, the spectral weights are *biased* towards the dominant configuration, and thus it should not come as much of a surprise that U $O_{4,5}$ NIXS and M_5 RIXS spectra of UGa_2 have recently been well simulated with an ionic U $5f^2$ model approach [24]. These kinds of methods are mostly sensitive to the main configuration and relevant symmetries of the system. We note that also an atomic $5f^2$ configuration can explain the magnetism in UGa_2 [24,33,63].

(2) Electron removal processes, like PES, promote an inversed order of the ionic configurations in the final state due to the uncompensated core-hole potential $U_{\rm fc}$. These spectroscopies are characterized by shake-up and satellite structures. In the case of U intermetallics, the spectral weights are determined by both the $5f^2$ and $5f^3$ configurations, making such a spectroscopy truly sensitive to covalence.

As a service to the reader, we provide a simple demonstration of these effects on the spectra in Appendix 3. We construct a simple two-level toy-model for UGa_2, and present the effects of the relevant intra- ($U_{\rm ff}$) and intershell ($U_{\rm fc}$) Coulomb interactions on the final state total energy diagram and on the redistribution of spectral weights. We also consider the effect that an increased hopping has on the toy model, so as to mimic a more itinerant system like UB_2. We conclude, the hybridization and covalence effects in U intermetallics are so strong that simple cluster calculations can no longer describe the PES core-level spectra as, e.g., for Ce intermetallic compounds (see, e.g., Refs. [60–62,64,65]). For U intermetallics, the analysis of the PES core-level spectra is no longer intuitive and, as the present paper has shown, requires a full DFT + DMFT-based AIM calculation.

V. CONCLUSION

In summary, we have presented a material-specific DFT + DMFT calculation of two intermetallic model materials, UGa_2 and UB_2, representing the extreme ends of the U $5f$

(de)localization scale. The parameters, Hubbard $U_{\rm ff}$, Hund's J and, especially, the double counting correction $\mu_{\rm dc}$, were tuned to best reproduce the valence band photoelectron spectroscopy data. Data from different incident photon energies enabled the disentanglement of subshells due to the different energy dependencies of the respective photoionization cross-sections. With the chosen parameters, the satellite structures of the U 4f core-level spectra were also well reproduced, requiring only the adjustment of the core-valence interaction $U_{\rm fc}$. The DFT + DMFT calculation revealed multiple U 5f atomic configurations contributing to the ground states of UGa_2 and UB_2, with the average valence being nearly identical for both compounds. However, the width of the atomic configuration histograms and the time dependence of the charge correlation functions allowed for the assessment of itinerancy; the 5f electrons in UB_2 were found to be much more itinerant than in UGa_2. This paper paves the way to a systematic classification of uranium intermetallic compounds: it establishes an experiment-guided DFT + DMFT quantitative assessment of the charge state in this class of materials, as well as a quantitative simulation of the U 4f core-level spectra based on the Anderson impurity model coupled to the DFT + DMFT hybridization function. We argue that different spectroscopic techniques should yield consistent results for the charge state of uranium in intermetallics and that the key ingredient is the proper inclusion of the electron correlation effects at the U sites relative to the itinerancy.

ACKNOWLEDGMENTS

A.H. was supported by JSPS KAKENHI Grants No. 21K13884, No. 21H01003, No. 23K03324, No. 23H03816, No. 23H03817, and the 2023 Osaka Metropolitan University (OMU) Strategic Research Promotion Project for Younger Researcher. A part of the computational calculations were performed at the Vienna Scientific Cluster (VSC). A.S. and M.M.F.C. greatly acknowledge funding from the German Research Foundation (DFG) Grant No. 387555779 and D.T. acknowledges support by the German Research Foundation (DFG) under the Walter Benjamin Programme, Project No. 521584902. J.K. was supported by the project Quantum Materials for Applications in Sustainable Technologies (QM4ST), funded by Project No. CZ.02.01.01/00/22_008/0004572 by Programme Johannes Amos Commenius, call Excellent Research. L.H. and A.V.A. benefited from support of the Czech Science Foundation, Project No. 21-09766S and A.V.A. thanks further the Ferroic Multifunctionalities Project No. CZ.02.01.01/00/22_008/0004591. We also acknowledge DESY, a member of the Helmholtz Association HGF, for access to beamtime and support from the Max Planck-POSTECH- Hsinchu Center for Complex Phase Materials.

APPENDIX

1. Finding $U_{\rm ff}$, J and $\mu_{\rm dc}$ with valence band spectra

Figure 7 summarizes the parameter dependence of the DFT + DMFT valence-band spectra for UGa_2. Analogous arguments can be made for UB_2. The gray vertical lines indicate the valence-band features (A to F) in the experimental PES data, see Figs. 2(a) and 2(b). We used 2.0 eV and 0.59 eV as starting values for Hubbard $U_{\rm ff}$ and Hund's J, respectively, values that were used in the DFT + DMFT study of Chatterjee and Kolorenč [56]. The J value corresponds to 80% of the Hartree-Fock value of the U 5f^3 configuration [66]. Around these $U_{\rm ff}$ and J values, we performed DMFT valence-band calculations for an extensive range of the double-counting correction $\mu_{\rm dc}$ values. For a given set of $U_{\rm ff}$ and J, the $\mu_{\rm dc}$ parameter controls the energy difference between U 5f and uncorrelated states. Thus, in the calculation, the energy positions that correspond to, e.g., the Ga 4s features E and F are almost linearly shifted to higher binding energies with increasing $\mu_{\rm dc}$.

The double-counting correction $\mu_{\rm dc}$, however, depends on the choice of $U_{\rm ff}$ and J values because it is intended to subtract the electron-electron interaction effects present in the DFT result on the mean-field level. Thus, in Fig. 7, the $\mu_{\rm dc}$-dependent spectra for different sets of $U_{\rm ff}$ and J are arranged in a matrix manner, such that in each row the calculated F feature appears at a similar binding energy. This demonstrates that one can find values for $\mu_{\rm dc}$ that reproduce the high-energy valence-band features for any set of $U_{\rm ff}$ and J. However, the choice of $U_{\rm ff}$ and J affects the U 5f features through the f–f interaction. It is important to note for $U_{\rm ff} = 3.0$ eV and $J = 0.59$ eV additional good agreement with the experimental U 5f features A and B is obtained.

2. $\mu_{\rm dc}$ dependence of the atomic configuration histograms

Figure 8 shows the variation of the atomic configuration histograms of UGa_2 and UB_2 with $\mu_{\rm dc}$. The double-counting correction renormalizes the energy position of the U 5f states, thus having a large impact on the valence distribution. This is particularly evident for UGa_2, where the distribution is very narrow for a shallower U 5f, e.g., for $\mu_{\rm dc}$=3.50 eV, the 5f^2 configuration strongly dominates (73.7%), while for deeper 5f states, e.g., for $\mu_{\rm dc}$=5 eV, the f^2 and f^3 configurations contribute almost equally to the ground state.

3. Toy model for comparing core-level PES and XAS

We consider a two-level *initial state* Hamiltonian $\hat{H}$ consisting of f^2 and $|f^3\underline{L}\rangle$ configurations, with $\underline{L}$ representing a valence hole. The two levels are separated by the charge transfer energy Δ and are coupled by the hopping amplitude t [see initial Fig. 9(a)] [60–62]. In the toy model,

$$\hat{H} = \begin{pmatrix} 0 & t \\ t & \Delta \end{pmatrix},$$

the ground state $|g\rangle = \alpha|f^2\rangle + \beta|f^3\underline{L}\rangle$ with coefficients α and β is determined by ratio t/Δ. We select t/Δ=0.822, resulting in the average 5f occupation $n_{5f} = 2.24$ for UGa_2 and UB_2 that was obtained in the main text, with α^2 and β^2 amounting to 0.76 and 0.24, respectively.

In the following, two cases will be discussed: (1) How $U_{\rm fc}$, for a fixed choice of t and Δ, and fixed ratio of $U_{\rm ff}/U_{\rm fc}$ in the case of XAS, impacts the satellites in core-level PES and XAS. (2) How t and Δ, for the same ratio t/Δ=0.822 and a given set of $U_{\rm ff}$ and $U_{\rm fc}$, impact the core level satellite in PES and XAS.

Case (1): The final states of the core-level PES and XAS processes are characterized by the presence of a core hole,

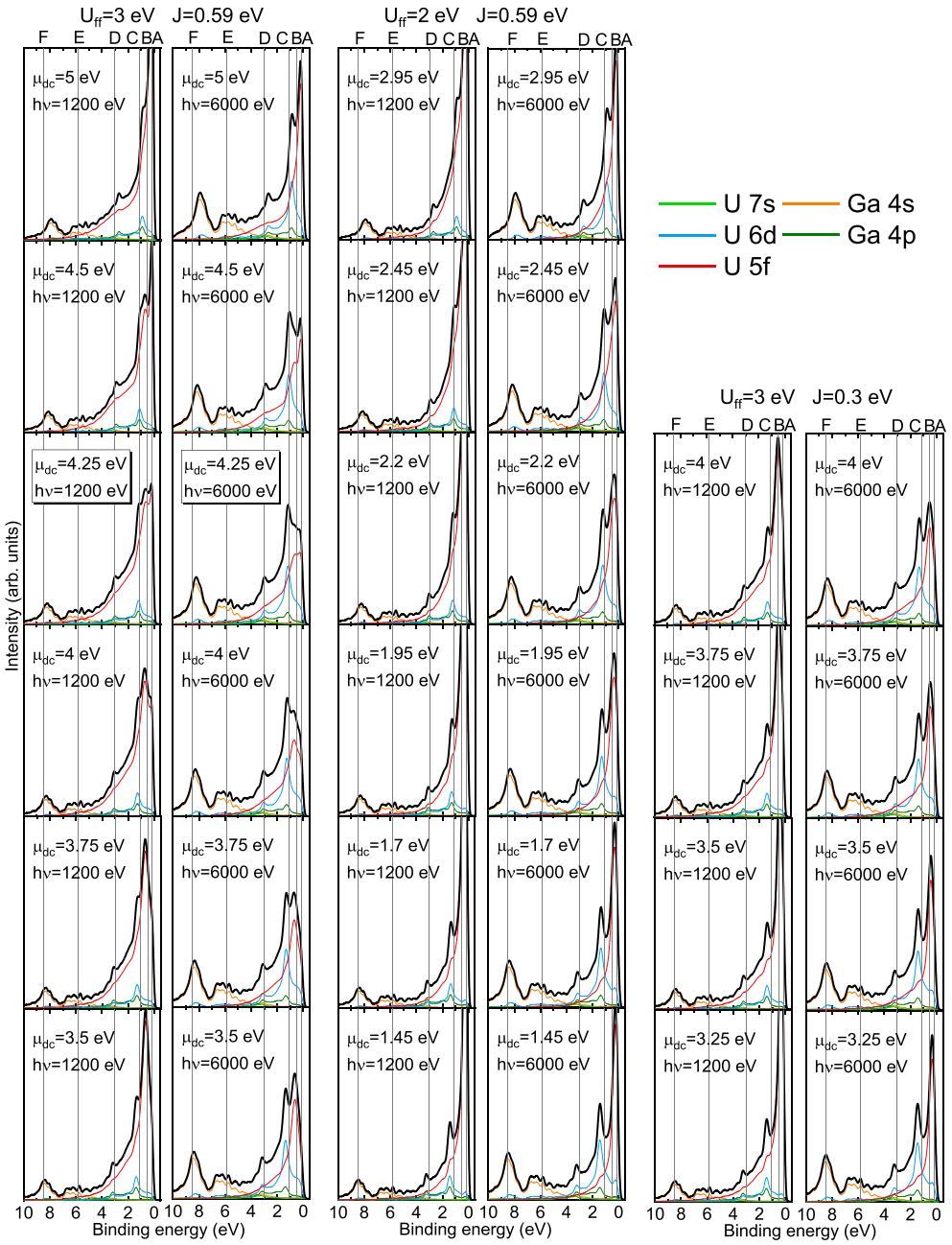

FIG. 7. $U_{\rm ff}$ and $\mu_{\rm dc}$ dependence of the DFT + DMFT valence band spectra of UGa_2. The vertical lines denote the energy position of the experimental features *A*–*F*, see labeling at top of figure and compare to Figs. 2(a) and 2(b). The panels with the optimal value of the parameters fitting the experimental spectra are marked by a frame and show the same calculation as Figs. 2(e) and 2(f).

necessitating consideration of the core-valence interaction $U_{\rm fc}$ between a core hole ($\underline{c}$) and $5f$ valence electrons.

In the PES *final state*, charge neutrality is broken. The basis is formed by $|\underline{c}f^2\rangle$ and $|\underline{c}f^3\underline{L}\rangle$ and the Hamiltonian $\hat{H}_{\rm PES}$ reads

$$\hat{H}_{\rm PES} = \begin{pmatrix} 0 & t \\ t & \Delta - U_{\rm fc} \end{pmatrix}.$$

In the final state, the configurations $|\underline{c}f^3\underline{L}\rangle$ and $|\underline{c}f^2\rangle$ are separated by $\Delta - U_{\rm fc}$ [see *final state PES* in Fig. 9(a)] and red and green ticks in the left panel of Fig. 9(b). Choosing Δ=1.75 eV with t=1.4373 eV, maintaining the ratio t/Δ=0.822, we calculate the core-level spectra for several values of $U_{\rm fc}$ between 0 and 6 eV [see left panel of Fig. 9(b)]. The exercise shows the sensitivity of peak positions and intensity ratios to $U_{\rm fc}$ for a given t and Δ. For $U_{\rm fc}$=0, the energy separation of the red and green ticks is given by Δ. With increasing $U_{\rm fc}$, the levels eventually cross when $\Delta - U_{\rm fc}$ becomes negative, i.e., the order of configurations is reversed with respect to the initial state. For $U_{\rm fc}$=5 eV [see blue curve in Fig. 9(b)], the value used in the present DFT + DMFT calculations, the toy model mimics the strong satellite of the $4f_{7/2}$ PES spectrum of UGa_2 in Fig. 6. With $U_{\rm fc}$ larger than Δ, the order of states is thus reversed in UGa_2. We note that this is actually a typical situation for the core-level spectra of f electron materials.

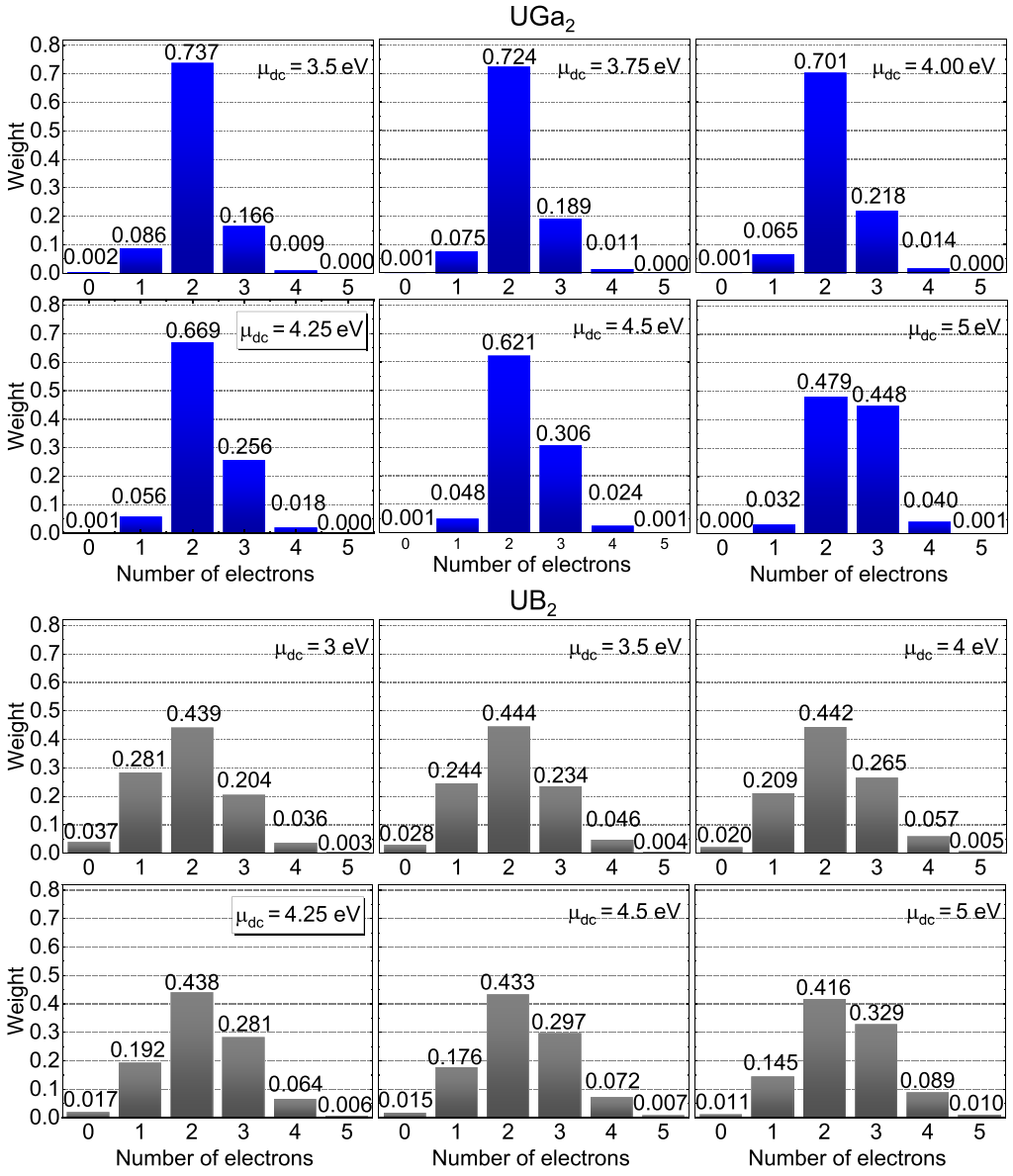

FIG. 8. μ_{dc} dependence of the atomic configuration histograms of UGa_2 (top) and UB_2 (bottom), where $U_{ff} = 3$ eV and $J = 0.59$ eV. The panels with the optimal value of the parameters fitting the experimental spectra are marked by a frame and show the same data as Figs. 4(a) and 4(b).

The relative spectral weights in the final state are not equal to the relative abundances β^2 and α^2 in the initial state. The transfer of spectral weight originates from the superposition (quantum-mechanical interference) of the f^2- and f^3-derived states in both the initial and final states. Therefore, the PES spectra cannot be modeled with an f^2 ionic model, even though the f^2 dominates the initial state. The reversed order of the configurations in the final state leads to substantial redistribution of spectral intensities. Only in the limit of very large U_{fc} or very small t would the PES intensities correspond to the weights of the initial state configurations. However, for uranium intermetallics both covalence and Coulomb interaction must be treated on the same footing.

For the charge neutral process in XAS, the basis is formed by $|\underline{c}f^3\rangle$ and $|\underline{c}f^4\underline{L}\rangle$, and the Hamiltonian $\hat{H}_{XAS}$ reads

$$\hat{H}_{XAS} = \begin{pmatrix} 0 & t \\ t & \Delta - U_{fc} + U_{ff} \end{pmatrix}.$$

For the $|\underline{c}f^4\underline{L}\rangle$ configuration, the energy gain due to U_{fc} is compensated by the extra f–f Coulomb repulsion U_{ff} due to the extra (photoexcited) f electron [see *final state XAS* in Fig. 9(a)]. Typically, U_{fc} is larger than U_{ff}, but they are of the same order of magnitude. Thus, in XAS, the levels in the final state have the same order as in the initial state, unlike in PES [see red and green ticks in right panel of Fig. 9(b)].

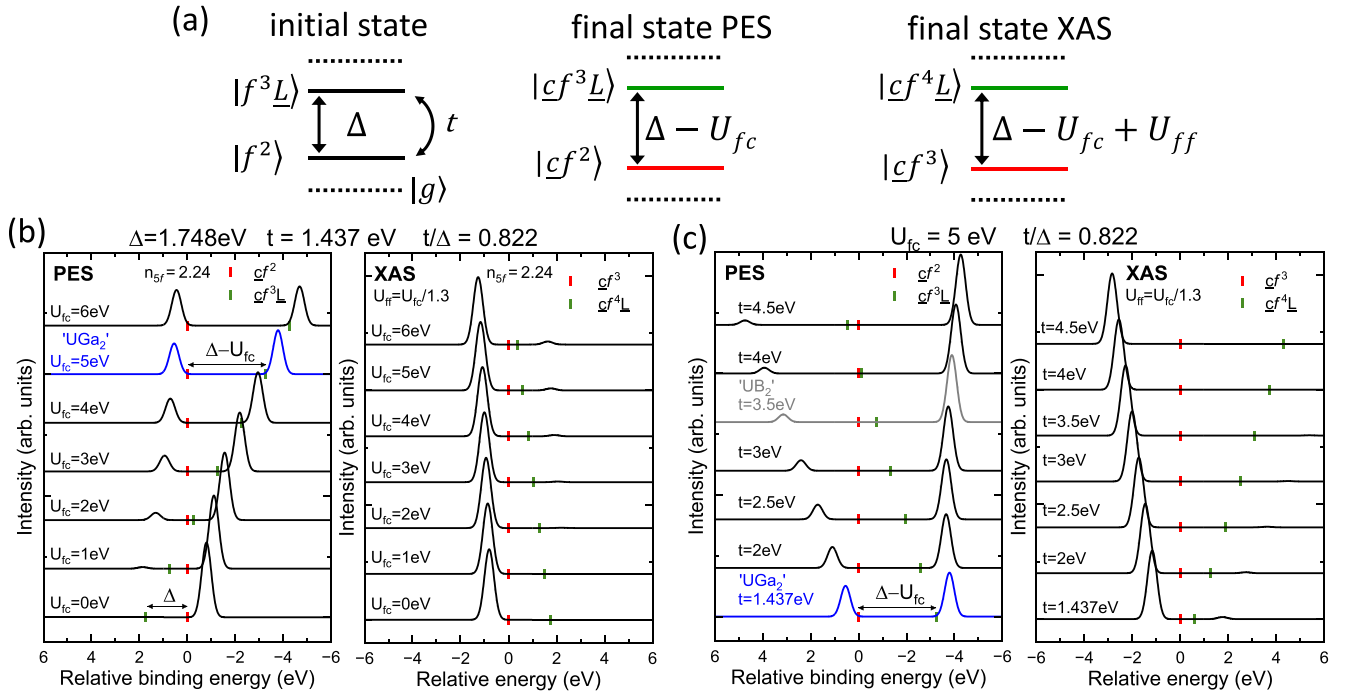

FIG. 9. (a) Schematic energy diagram displaying the initial state problem with ground state $|g\rangle = \alpha|f^2\rangle + \beta|f^3\underline{L}\rangle$, and PES and XAS final states. (b) Core-level ($\underline{c}$) PES and XAS spectra in the two-configuration toy model, maintaining the same average $5f$ filling, for various core-valence interaction values $U_{\rm fc}$ and a fixed small hopping t (and small Δ) addressing the UGa_2 electronic structure problem (see blue spectrum). (c) Core-level PES and XAS spectra in the two-configuration toy model, maintaining the same average $5f$ filling, for several values of hopping t (and Δ) with fixed U_{fc}=5 eV, addressing the problem of UB_2 (see gray spectrum). The red and green ticks mark the energy positions of the nonhybridized final states.

We fix the parameter $U_{\rm ff}$ to $U_{\rm fc}/1.3$ and then calculate the XAS spectra for several values of $U_{\rm fc}$ between 0 and 6 eV [see Fig. 9(b)]. The main line and satellite are composed largely of $|\underline{c}f^3\rangle$ and $|\underline{c}f^4\underline{L}\rangle$, respectively, with the main line consistently dominating the spectrum, despite the mixture of f^2 and f^3 in the initial state. Hence, XAS spectra reflect the dominant f^2 configuration. In contrast to PES, the satellites are never very large and peak positions and intensities are fairly insensitive to $U_{\rm fc}$. In case $U_{\rm ff}$=$U_{\rm fc}$, the satellite intensity would even be zero for all values of $U_{\rm fc}$

Therefore, an ionic model considering only the formal f^2 configuration provides a valid description for core-level XAS (similarly for NIXS) in uranium intermetallic compounds.

Case (2): Now, we discuss the impact of t and Δ with a fixed t/Δ of 0.822 to maintain the same $5f$ occupation. We now fix $U_{\rm fc}$=5 eV and vary t (and Δ) from 1.437 eV, the value mimicking the case of UGa_2 [see blue curve in Fig. 9(c)], to t=4.5 eV. Again, we observe a strong dependence of position and intensity ratios on the actual size of t (and Δ). The hopping of t=3.5 eV mimics the PES core-level data of UB_2 [see gray curve in Fig. 9(c)]. For even larger values of t (and Δ), the satellite becomes even smaller and the order of states reverses back to the same order as in the initial state. In XAS, as before, the spectra exhibit only one major line and a negligible satellite spectral weight, the latter becoming even less pronounced the larger Δ becomes with respect to $U_{\rm fc}$ and $U_{\rm ff}$.

[1] C. Pfleiderer, Superconducting phases of f-electron compounds, Rev. Mod. Phys. **81**, 1551 (2009).

[2] M. Brando, D. Belitz, F. M. Grosche, and T. R. Kirkpatrick, Metallic quantum ferromagnets, Rev. Mod. Phys. **88**, 025006 (2016).

[3] J. A. Mydosh, P. M. Oppeneer, and P. S. Riseborough, Hidden order and beyond: An experimentaltheoretical overview of the multifaceted behavior of URu_2Si_2, J. Phys.: Condens. Matter **32**, 143002 (2020).

[4] S. K. Lewin, C. E. Frank, S. Ran, J. Paglione, and N. P. Butch, A review of UTe_2 at high magnetic fields, Rep. Prog. Phys. **86**, 114501 (2023).

[5] K. Haule and G. Kotliar, Arrested Kondo effect and hidden order in URu_2Si_2, Nat. Phys. **5**, 796 (2009).

[6] H.-H. Kung, R. E. Baumbach, E. D. Bauer, V. K. Thorsmølle, W.-L. Zhang, K. Haule, J. A. Mydosh, and G. Blumberg, Chirality density wave of the "hidden order" phase in URu_2Si_2, Science **347**, 1339 (2015).

[7] L. Miao, R. Basak, S. Ran, Y. Xu, E. Kotta, H. He, J. D. Denlinger, Y.-D. Chuang, Y. Zhao, Z. Xu, J. W. Lynn, J. R. Jeffries, S. R. Saha, I. Giannakis, P. Aynajian, C.-J. Kang, Y. Wang, G. Kotliar, N. P. Butch, and L. A. Wray, High temperature singlet-based magnetism from Hund's rule correlations, Nat. Commun. **10**, 644 (2019).

[8] L. Miao, S. Liu, Y. Xu, E. C. Kotta, C.-J. Kang, S. Ran, J. Paglione, G. Kotliar, N. P. Butch, J. D. Denlinger, and L. A. Wray, Low energy band structure and symmetries of UTe_2 from angle-resolved photoemission spectroscopy, Phys. Rev. Lett. **124**, 076401 (2020).

[9] K. Haule, Exact double counting in combining the dynamical mean field theory and the density functional theory, Phys. Rev. Lett. **115**, 196403 (2015).

[10] J. R. Jeffries, K. T. Moore, N. P. Butch, and M. B. Maple, Degree of $5f$ electron localization in URu_2Si_2: Electron energy-loss spectroscopy and spin-orbit sum rule analysis, Phys. Rev. B **82**, 033103 (2010).

[11] S.-i. Fujimori, T. Ohkochi, I. Kawasaki, A. Yasui, Y. Takeda, T. Okane, Y. Saitoh, A. Fujimori, H. Yamagami, Y. Haga, E. Yamamoto, Y. Tokiwa, S. Ikeda, T. Sugai, H. Ohkuni, N. Kimura, and Y. Onuki, Electronic structure of heavy fermion uranium compounds studied by core-level photoelectron spectroscopy, J. Phys. Soc. Jpn. **81**, 014703 (2012).

[12] L. A. Wray, J. Denlinger, S. W. Huang, H. He, N. P. Butch, M. B. Maple, Z. Hussain, and Y. D. Chuang, Spectroscopic determination of the atomic f-electron symmetry underlying hidden order in URu_2 Si_2, Phys. Rev. Lett. **114**, 236401 (2015).

[13] C. H. Booth, S. A. Medling, J. G. Tobin, R. E. Baumbach, E. D. Bauer, D. Sokaras, D. Nordlund, and T.-C. Weng, Probing $5f$-state configurations in URu_2 Si_2 with U L_{III}-edge resonant x-ray emission spectroscopy, Phys. Rev. B **94**, 045121 (2016).

[14] M. Sundermann, M. W. Haverkort, S. Agrestini, A. Al-Zein, M. Moretti Sala, Y. Huang, M. Golden, A. de Visser, P. Thalmeier, L. H. Tjeng, and A. Severing, Direct bulk-sensitive probe of $5f$ symmetry in URu_2 Si_2, Proc. Natl. Acad. Sci. USA **113**, 13989 (2016).

[15] K. O. Kvashnina, H. C. Walker, N. Magnani, G. H. Lander, and R. Caciuffo, Resonant x-ray spectroscopy of uranium intermetallics at the $M_{4,5}$ edges of uranium, Phys. Rev. B **95**, 245103 (2017).

[16] S.-i. Fujimori, I. Kawasaki, Y. Takeda, H. Yamagami, A. Nakamura, Y. Homma, and D. Aoki, Electronic structure of UTe_2 studied by photoelectron spectroscopy, J. Phys. Soc. Jpn. **88**, 103701 (2019).

[17] S. M. Thomas, F. B. Santos, M. H. Christensen, T. Asaba, F. Ronning, J. D. Thompson, E. D. Bauer, R. M. Fernandes, G. Fabbris, and P. F. S. Rosa, Evidence for a pressure-induced antiferromagnetic quantum critical point in intermediate-valence UTe_2, Sci. Adv. **6**, eabc8709 (2020).

[18] S.-i. Fujimori, I. Kawasaki, Y. Takeda, H. Yamagami, A. Nakamura, Y. Homma, and D. Aoki, Core-level photoelectron spectroscopy study of UTe_2, J. Phys. Soc. Jpn. **90**, 015002 (2021).

[19] A. B. Shick, S.-I. Fujimori, and W. E. Pickett, UTe_2: A nearly insulating half-filled $j = \frac{5}{2} 5f^3$ heavy-fermion metal, Phys. Rev. B **103**, 125136 (2021).

[20] D. Aoki, H. Sakai, P. Opletal, Y. Tokiwa, J. Ishizuka, Y. Yanase, H. Harima, A. Nakamura, D. Li, Y. Homma, Y. Shimizu, G. Knebel, J. Flouquet, and Y. Haga, First observation of the de Haas-van Alphen effect and Fermi surfaces in the unconventional superconductor UTe_2, J. Phys. Soc. Jpn. **91**, 083704 (2022).

[21] S. Liu, Y. Xu, E. C. Kotta, L. Miao, S. Ran, J. Paglione, N. P. Butch, J. D. Denlinger, Y.-D. Chuang, and L. A. Wray, Identifying f-electron symmetries of UTe_2 with O-edge resonant inelastic x-ray scattering, Phys. Rev. B **106**, L241111 (2022).

[22] F. Wilhelm, J.-P. Sanchez, D. Braithwaite, G. Knebel, G. Lapertot, and A. Rogalev, Investigating the electronic states of UTe_2 using x-ray spectroscopy, Commun. Phys. **6**, 96 (2023).

[23] D. S. Christovam, M. Sundermann, A. Marino, D. Takegami, J. Falke, P. Dolmantas, M. Harder, H. G. amd Bernhard Keimer, A. Gloskovskii, M. W. Haverkort, I. Elfimov, G. Zwicknagl, A. V. Andreev, L. Havela, M. M. Bordelon, E. D. Bauer, P. F. S. Rosa, A. Severing, and L. H. Tjeng, Stabilization of U $5f^2$ configuration in UTe_2 through U $6d$ dimers in the presence of Te2 chains, arXiv:2402.03852.

[24] A. Marino, M. Sundermann, D. S. Christovam, A. Amorese, C.-F. Chang, P. Dolmantas, A. H. Said, H. Gretarsson, B. Keimer, M. W. Haverkort, A. V. Andreev, L. Havela, P. Thalmeier, L. H. Tjeng, and A. Severing, Singlet magnetism in intermetallic UGa_2 unveiled by inelastic x-ray scattering, Phys. Rev. B **108**, 045142 (2023).

[25] M. B. Trzhaskovskaya, V. Nefedov, and V. Yarzhemsky, Photoelectron angular distribution parameters for elements $Z = 1$ to $Z = 54$ in the photoelectron energy range 1005000 eV, At. Data Nucl. Data Tables **77**, 97 (2001).

[26] M. B. Trzhaskovskaya, V. Nefedov, and V. Yarzhemsky, Photoelectron angular distribution parameters for elements $Z = 55$ to $Z = 100$ in the photoelectron energy range 1005000 ev, At. Data Nucl. Data Tables **82**, 257 (2002).

[27] M. Trzhaskovskaya, V. Nikulin, V. Nefedov, and V. Yarzhemsky, Non-dipole second order parameters of the photoelectron angular distribution for elements $Z = 1100$ in the photoelectron energy range 1–10 keV, At. Data Nucl. Data Tables **92**, 245 (2006).

[28] E. S. Makarov and V. A. Ledvik, Crystal structure of uranium digallium (UGa_2), Sov. Phys. Crystallogr. **1**, 506 (1956).

[29] A. V. Andreev, K. P. Belov, A. V. Deryagin, Z. A. Kazei, R. Z. Levitin, A. Menovsky, Y. F. Popov, and V. I. Silantev, Crystal structure, and magnetic and magnetoelastic properties of UGa_2, Sov. Phys. JETP **48**, 1187 (2001).

[30] J.-P. Dancausse, E. Gering, S. Heathman, U. Benedict, L. Gerward, S. Staun Olsen, and F. Hulliger, Compression study of uranium borides UB_2, UB_4 and U_{12} by synchrotron x-ray diffraction, J. Alloys Compd. **189**, 205 (1992).

[31] H. H. Hill, in *Plutonium 1970 and other Actinides*, edited by W. N. Miner (The Metallurgical Society of the AIME, New York, 1970), p. 2.

[32] A. Lawson, A. Williams, J. Smith, P. Seeger, J. Goldstone, J. O'Rourke, and Z. Fisk, Magnetic neutron diffraction study of UGa_3 and UGa_2, J. Magn. Magn. Mater. **50**, 83 (1985).

[33] T. Honma, Y. Inada, R. Settai, S. Araki, Y. Tokiwa, T. Takeuchi, H. Sugawara, H. Sato, K. Kuwahara, M. Yokoyama, H. Amitsuka, T. Sakakibara, E. Yamamoto, Y. Haga, A. Nakamura, H. Harima, H. Yamagami, and Y. nuki, Magnetic and Fermi surface properties of the ferromagnetic compound UGa_2, J. Phys. Soc. Jpn. **69**, 2647 (2000).

[34] E. Yamamoto, T. Honma, Y. Haga, Y. Inada, D. Aoki, N. Suzuki, R. Settai, H. Sugawara, H. Sato, and Y. Ōnuki, Electrical and thermal properties of UB_2, J. Phys. Soc. Jpn. **68**, 972 (1999).

[35] W.-D. Schneider and C. Laubschat, $5f$-electron localization in uranium compounds, Phys. Rev. Lett. **46**, 1023 (1981).

[36] T. Gouder, L. Havela, M. Diviš, J. Rebizant, P. Oppeneer, and M. Richter, Surface electronic structure of UGa_x films, J. Alloys Compd. **314**, 7 (2001).

[37] S.-I. Fujimori, M. Kobata, Y. Takeda, T. Okane, Y. Saitoh, A. Fujimori, H. Yamagami, Y. Haga, E. Yamamoto, and Y. Ōnuki, Manifestation of electron correlation effect in $5f$ states of uranium compounds revealed by $4d-5f$ resonant photoelectron spectroscopy, Phys. Rev. B **99**, 035109 (2019).

[38] S.-i. Fujimori, Y. Takeda, T. Okane, Y. Saitoh, A. Fujimori, H. Yamagami, Y. Haga, E. Yamamoto, and Y. Ōnuki, Electronic structures of uranium compounds studied by soft x-ray photoelectron spectroscopy, J. Phys. Soc. Jpn. **85**, 062001 (2016).

[39] A. V. Kolomiets, J.-C. Griveau, J. Prchal, A. V. Andreev, and L. Havela, Variations of magnetic properties of UGa_2 under pressure, Phys. Rev. B **91**, 064405 (2015).

[40] C. Schlueter, A. Gloskovskii, K. Ederer, I. Schostak, S. Piec, I. Sarkar, Y. Matveyev, P. Lömker, M. Sing, R. Claessen, C. Wiemann, C. M. Schneider, K. Medjanik, G. Schönhense, P. Amann, A. Nilsson, and W. Drube, The new dedicated HAXPES beamline P22 at PETRAIII, AIP Conf. Proc. **2054**, 040010 (2019).

[41] H.-M. Tsai, H.-W. Fu, C.-Y. Kuo, L.-J. Huang, C.-S. Lee, C.-Y. Hua, K.-Y. Kao, H.-J. Lin, H.-S. Fung, S.-C. Chung, C.-F. Chang, A. Chainani, L. H. Tjeng, and C.-T. Chen, A submicron soft x-ray active grating monochromator beamline for ultra-high resolution angle-resolved photoemission spectroscopy, AIP Conf. Proc. **2054**, 060047 (2019).

[42] H. Gretarsson, D. Ketenoglu, M. Harder, S. Mayer, F.-U. Dill, M. Spiwek, H. Schulte-Schrepping, M. Tischer, H.-C. Wille, B. Keimer, and H. Yavaş, IRIXS: A resonant inelastic x-ray scattering instrument dedicated to X-rays in the intermediate energy range, J. Synchrotron Radiat. **27**, 538 (2020).

[43] G. Kotliar, S. Y. Savrasov, K. Haule, V. S. Oudovenko, O. Parcollet, and C. A. Marianetti, Electronic structure calculations with dynamical mean-field theory, Rev. Mod. Phys. **78**, 865 (2006).

[44] A. Georges, G. Kotliar, W. Krauth, and M. J. Rozenberg, Dynamical mean-field theory of strongly correlated fermion systems and the limit of infinite dimensions, Rev. Mod. Phys. **68**, 13 (1996).

[45] P. Blaha, K. Schwarz, G. Madsen, D. Kvasnicka, and J. Luitz, *WIEN2k, An Augmented Plane Wave + Local Orbitals Program for Calculating Crystal Properties* (Karlheinz Schwarz, Techn. Universitat Wien, Austria, 2001).

[46] J. Kuneš, R. Arita, P. Wissgott, A. Toschi, H. Ikeda, and K. Held, Wien2wannier: From linearized augmented plane waves to maximally localized Wannier functions, Comput. Phys. Commun. **181**, 1888 (2010).

[47] A. A. Mostofi, J. R. Yates, G. Pizzi, Y.-S. Lee, I. Souza, D. Vanderbilt, and N. Marzari, An updated version of wannier90: A tool for obtaining maximally-localised wannier functions, Comput. Phys. Commun. **185**, 2309 (2014).

[48] P. Werner, A. Comanac, L. de' Medici, M. Troyer, and A. J. Millis, Continuous-time solver for quantum impurity models, Phys. Rev. Lett. **97**, 076405 (2006).

[49] E. Gull, A. J. Millis, A. I. Lichtenstein, A. N. Rubtsov, M. Troyer, and P. Werner, Continuous-time Monte Carlo methods for quantum impurity models, Rev. Mod. Phys. **83**, 349 (2011).

[50] L. Boehnke, H. Hafermann, M. Ferrero, F. Lechermann, and O. Parcollet, Orthogonal polynomial representation of imaginary-time Green's functions, Phys. Rev. B **84**, 075145 (2011).

[51] H. Hafermann, K. R. Patton, and P. Werner, Improved estimators for the self-energy and vertex function in hybridization-expansion continuous-time quantum Monte Carlo simulations, Phys. Rev. B **85**, 205106 (2012).

[52] M. Jarrell and J. Gubernatis, Bayesian inference and the analytic continuation of imaginary-time quantum Monte Carlo data, Phys. Rep. **269**, 133 (1996).

[53] M. Karolak, G. Ulm, T. Wehling, V. Mazurenko, A. Poteryaev, and A. Lichtenstein, Double counting in LDA + DMFT—The example of NiO, J. Electron Spectrosc. Relat. Phenom. **181**, 11 (2010).

[54] A. Hariki, T. Uozumi, and J. Kuneš, LDA+DMFT approach to core-level spectroscopy: Application to $3d$ transition metal compounds, Phys. Rev. B **96**, 045111 (2017).

[55] M. Winder, A. Hariki, and J. Kuneš, X-ray spectroscopy of the rare-earth nickelate $LuNiO_3$: LDA + DMFT study, Phys. Rev. B **102**, 085155 (2020).

[56] B. Chatterjee and J. Kolorenč, Electronic structure and magnetism in UGa_2: DFT + DMFT approach, Phys. Rev. B **103**, 205146 (2021).

[57] J. Yeh and I. Lindau, Atomic subshell photoionization cross sections and asymmetry parameters: $1 \leqslant Z \leqslant 103$, At. Data Nucl. Data Tables **32**, 1 (1985).

[58] A. Bosch, Photoelectron spectroscopy – New angle-resolved spectrometer and study of dilute alloys, Ph.D. thesis, University of Groningen, 1982.

[59] E. R. Ylvisaker, J. Kuneš, A. K. McMahan, and W. E. Pickett, Charge fluctuations and the valence transition in Yb under pressure, Phys. Rev. Lett. **102**, 246401 (2009).

[60] O. Gunnarsson and K. Schönhammer, Electron spectroscopies for Ce compounds in the impurity model, Phys. Rev. B **28**, 4315 (1983).

[61] T. J. A. Kotani and J. Parlebas, Many-body effects in core-level spectroscopy of rare-earth compounds, Adv. Phys. **37**, 37 (1988).

[62] F. de Groot, X-ray absorption and dichroism of transition metals and their compounds, J. Electron Spectrosc. Relat. Phenom. **67**, 529 (1994).

[63] M. Richter, M. Diviš, J. Forstreuter, K. Koepernik, L. Steinbeck, and H. Eschrig, Calculation of the paramagnetic susceptibility and specific heat in UGa_2 and UPd_2 Al_3 from ab initio crystal field theory, Physica B: Condens. Matter **230-232**, 519 (1997).

[64] M. Sundermann, F. Strigari, T. Willers, J. Weinen, Y. Liao, K.-D. Tsuei, N. Hiraoka, H. Ishii, H. Yamaoka, J. Mizuki, Y. Zekko, E. Bauer, J. Sarrao, J. Thompson, P. Lejay, Y. Muro, K. Yutani, T. Takabatake, A. Tanaka, N. Hollmann *et al.*, Quantitative study of the f occupation in $CeMIn_5$ and other cerium compounds with hard x-rays, J. Electron. Spectrosc. Relat. Phenom. **209**, 1 (2016).

[65] Y. Shimura, A. Wörl, M. Sundermann, S. Tsuda, D. T. Adroja, A. Bhattacharyya, A. M. Strydom, A. D. Hillier, F. L. Pratt, A. Gloskovskii, A. Severing, T. Onimaru, P. Gegenwart, and T. Takabatake, Antiferromagnetic correlations in strongly valence fluctuating CeIrSn, Phys. Rev. Lett. **126**, 217202 (2021).

[66] R. D. Cowan, *The Theory of Atomic Structure and Spectra* (University of California Press, Berkely and Los Angeles, 1981), Vol. 3.